AMBER data reduction

E Tatulli [a,b], G. Duvert [b]

[a] *INAF-Osservatorio Astrofisico di Arcetri, Istituto Nazionale di Astrofisica, Largo E. Fermi 5, I-50125 Firenze, Italy*

[b] *Laboratoire d'Astrophysique de Grenoble, UMR 5571 Université Joseph Fourier/CNRS, BP 53, F-38041 Grenoble Cedex 9, France*

Abstract

This course describes the data reduction process of the AMBER instrument, the three beam recombiner of the Very Large Telescope Interferometer (VLTI). In the body of the paper, we develop its principles from a theoretical point of view and we illustrate the main points with examples taken from the practical AMBER data reduction session given during the school. The detailed practical application making use of the ESO `gasgano` tool is then presented in Appendix. In this lecture, we particularly emphasize that the AMBER data reduction process is (i) a fit of the interferogram in the detector plane, (ii) using an *a priori* calibration of the instrument, where (iii) the complex visibility of the source is estimated from a least-square determination of a linear inverse problem, and where (iv) the derived AMBER observables are the squared visibility, the closure phase, and the spectral differential phase.

1 Introduction

The AMBER instrument is the first generation of near-infrared three beam recombiner of the Very Large Telescope Interferometer (VLTI), which offers a combination of characteristics that, though they can be found distributed in other interferometers, are all brought together in the same instrument for the first time. These characteristics can be categorized as follows: AMBER/VLTI is

(1) a single-mode waveguided interferometer: in order to perform spatial filtering of the turbulent wavefront

(2) a multiaxial "all-in-one" recombination scheme (Tatulli and LeBouquin, 2006), where the fringes are spatially coded on the detector and recorded all together in the same interference pattern

(3) a 2/3 beam-recombiner in the J (1.25μm), H (1.65μm) and K (2.2μm) bands, that can make use of the 8 meters Unitary Telescopes (UTs) or the 1.8 meters auxiliary Telescopes (ATs) provided by the VLT, and can achieve a maximal spatial resolution of $\theta \sim 2$mas

(4) a spectrograph, allowing spectral resolutions of $\mathcal{R} = 35, 1500, 10000$

For a thorough description of the instrument, we refer the interested readers to the paper of M. Wittkowski, "MIDI and AMBER from the user's point of view", in this issue. However, it is important to recall here that, from a signal processing point of view, the process of image formation in the case of AMBER has to be described in 3 majors steps: *(i) spatial filtering; (ii) beam recombination; (iii) spectral dispersion*, as it is summarized in Fig. 4 and 5 of Wittkowski's paper.

In this specific lecture, we concentrate on the two major questions that arise when dealing with the data reduction of the AMBER instrument: what is the influence of the AMBER specific instrumental design on the recorded interferometric signal? and conversely, how can we use the specificities of this signal to derive an optimized signal processing of the data? Following the previous enumeration of AMBER characteristics, these two questions can be address according to 3 themes that will be the framework of this coursebook:

(1) what is the effect in single-mode waveguides on the interferometric signal and how can we make use of this in the amber data reduction process? (Section 2)

(2) what is the proper AMBER interferometric equation and what is specific about it? (Section 3)

(3) + (4) what are the AMBER observables and how can we estimate them? (Section 4)

The following appendix is then dedicated to a practical application of AMBER data reduction principles with the ESO `gasgano` tool, as it was presented during the AMBER practical session of the Goutelas school.

2 Spatial filtering and visibility

The interest of using the practical characteristics of single-mode fibers to carry and recombine the light (as opposed to bulk optics), as first proposed by Connes et al. (1987) with his conceptual FLOAT interferometer, is now well established. Furthermore, in the light of the FLUOR experiment on the IOTA

interferometer, which demonstrated the "on-sky" feasibility of such interferometers for the first time, Coudé Du Foresto et al. (1997) showed that making use of single mode waveguides could also increase the performances of optical interferometry, thanks to their remarkable properties of spatial filtering, which change the phase fluctuations of the atmospheric turbulent wavefront into intensity fluctuations. Indeed, and as schematically shown by Fig. 1, the effect of the single-mode waveguide is to only propagate in its core the part of the incoming electric-field projected on its first mode. As a result the wavefront at the output of the fiber is perfectly plane. In the image plane (see Fig. 2) this means that the shape of the signal at the output of the waveguide is *fully deterministic* (as a matter of fact quasi-Gaussian, e.g. Mège et al. (2003)), as opposed to multimode instruments where the short-exposed images are presenting the well-known randomly distributed speckle pattern. And the fact that at the fiber's output, the intensity profile is deterministic, that is *calibratable*, is of high interest for the AMBER data reduction process. Indeed this important information can be used as an *a priori*, therefore improving the performances of the signal processing. We will come back to this point in the next chapters.

The obvious trade-off in producing perfectly stable intensity profile from single-mode waveguide is that only a fraction of the light, namely the coupling coefficient, is entering the fiber (once again, as opposed to multimode experiments where the number of photons remains constant if we neglect the scintillation, see Fig. 2). This coupling coefficient depends not only on the source's extent (Dyer and Christensen, 1999) but also on the turbulence, more precisely the Strehl ratio (Coudé du Foresto et al., 2000). This explains why single-mode interferometers are also requiring telescopes equipped with Adaptive Optics systems, in order to optimize the fraction of flux entering the fiber. Nonetheless, this coupling coefficient property has a strong impact on the estimated visibility. Indeed this latter will be biased both by geometric (static) and atmospheric (turbulent) effects. To cope with this situation Coudé Du Foresto et al. (1997) proposed to monitor the coupling coefficient fluctuations in real time thanks to dedicated photometric outputs and to perform instantaneous photometric calibration. And indeed, he experimentally proved that doing so, single-mode interferometry could achieve visibility measurements with precisions of 1% or lower *on compact sources*.

Later, from its theoretical work, Mège et al. (2001) has finally shown that, in the general case of partial correction by adaptive optics and for a source with a given spatial extent, the measured instantaneous visibility could be expressed in the general case as $V_{ij} \propto \text{TF}[O_\star(\alpha)L^{ij}(\alpha)]$, that is the Fourier Transform of the object brilliance distribution *multiplied by the instantaneous interferometric antenna lobe, which is turbulent*. This straightforward explains why and how the visibility is biased by geometric effect (lobe effect such as in radio-interferometry) and by the turbulence, and why, as one of the conse-
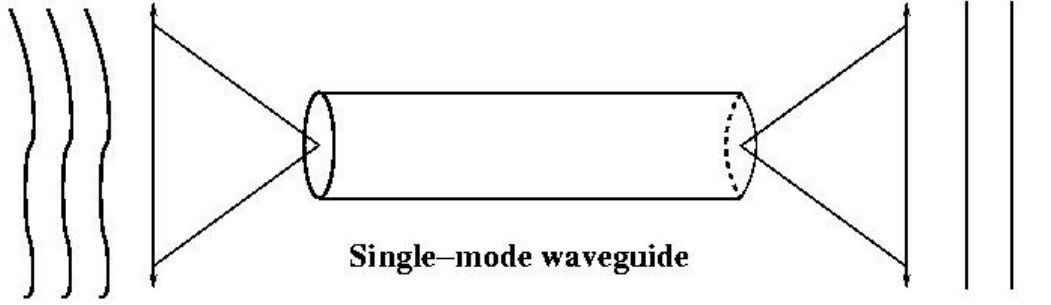
Fig. 1. Schematic pupil plane view of the effect of single-mode waveguides on the turbulent wavefront: at the entrance of the fiber, the wavefront is corrugated by the atmospheric turbulence + static aberrations of the instrument. At the output, only the projection of the electric field on the first mode of the waveguide has propagated and as a consequence, the wavefront is plane.
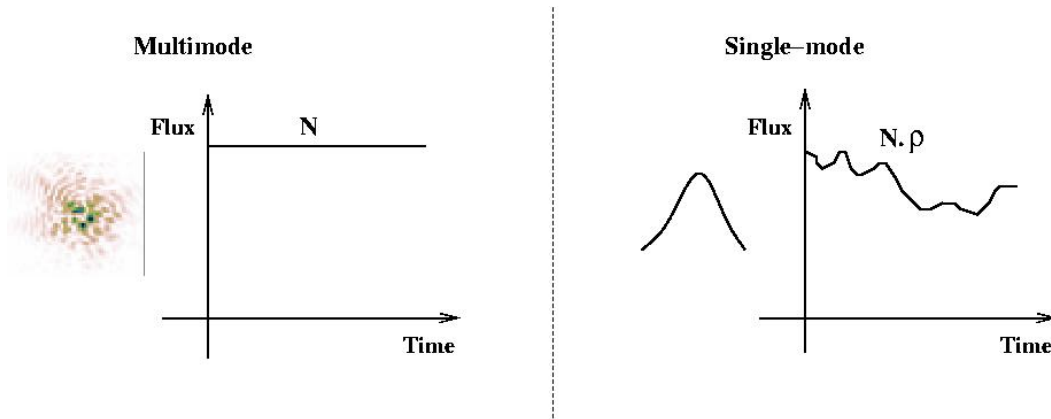

Fig. 2. Schematic image plane view of the effect of single-mode waveguides on the image. In the multimode case (left), the image is the well-known randomly distributed speckle pattern. But the total number of photons in the image is constant (scintillation neglected). In the single-mode case (right), the image is deterministic (Gaussian-like shaped) but the total number of photons depends on the coupling coefficient (ρ) which varies with the turbulence.

quence, the field of view of single-mode interferometers is limited to one Airy disk, that is $\Theta \sim \lambda/D$, where D is the diameter of one telescope. This also tells that strictly speaking, the modal visibility is not the source visibility. However, Tatulli et al. (2004) confirmed from a analytical approach that, in the specific case of compact objects such as dealt by Coudé Du Foresto et al. (1997), the benefit of single-mode waveguides is substantial, not only in terms of the signal-to-noise ratio of the visibility but also of the robustness of the estimator. From now on, we will consider our observable to be the complex modal visibility.

4

3 Characterizing the instrument

The aim of this section is to put in equations the characteristics of the AMBER interferometric signal, hence to emphasize the importance of acquiring calibration files describing the AMBER specific instrumental setup before (or after) recording science data. For sake of clarity, the notations which will be used all along this Section to derive the AMBER interferometric equation are summarized in Appendix A.

3.1 Building the AMBER interferometric equation

The following demonstration is given considering a generic $N_{tel} \geq 2$ telescope interferometer. In the specific case of AMBER, however, $N_{tel} = 2$ or $N_{tel} = 3$. Each line of the detector being independent of each other, we can focus our attention on one single spectral channel, which is assumed to be monochromatic here. The effect of a spectral bandwidth on the interferometric equation is treated in Sect. 4.2.

Interferometric output:
one beam lit (table 1, top): when only the ith beam is illuminated, the signal recorded in the interferometric channel is the photometric flux F^i spread on the Airy pattern a_k^i
two beams lit: (table 1, middle): When beams i and j are illuminated simultaneously, the coherent addition of both beams results in an interferometric component superimposed on the photometric continuum. The interferometric part, i.e. the fringes, arises from the amplitude modulation of the coherent flux F_c^{ij} at the coding frequency f^{ij}
*all beams lit: (table 1, bottom)*: Such an analysis can be done for each pair of beams arising from the interferometer. As a result, the interferogram recorded on the detector can be written in the general form:

$$i_k = \sum_i^{N_{tel}} a_k^i F^i + \sum_{i<j}^{N_{tel}} \sqrt{a_k^i a_k^j} C_B^{ij} \mathrm{Re} \left[F_c^{ij} \mathrm{e}^{i(2\pi\alpha_k f^{ij} + \phi_s^{ij} + \Phi_B^{ij})} \right] \tag{1}$$

Here, ϕ_s^{ij} is the instrumental phase taking possible misalignment and/or differential phase between the beams a_k^i and a_k^j into account, and C_B^{ij} and Φ_B^{ij} are, respectively, the loss of contrast and the phase shift due to polarization mismatch between the two beams (after the polarizers), such as the rotation of the single-mode fibers might induce. This equation is governing the AMBER fringe pattern, that is the interferometric channel of the fourth column of the detector (e.g. in figures of table 1). The first sum in Eq. (1), which represents the continuum part of the interference pattern, is called the DC component
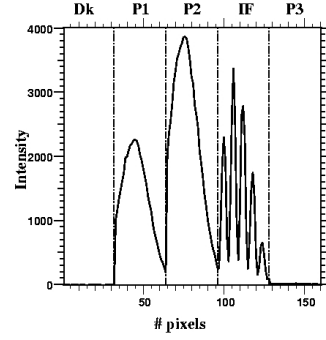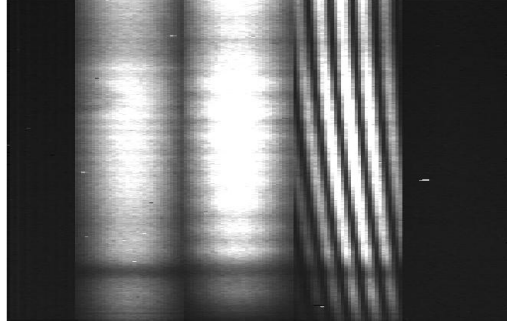
Table 1

Image of the detector (left) and cut along one spectral channel (right). Below each plot are given equations ruling photometric (when illuminated) and interferometric channels. From top to bottom: one, two and all beams lit.
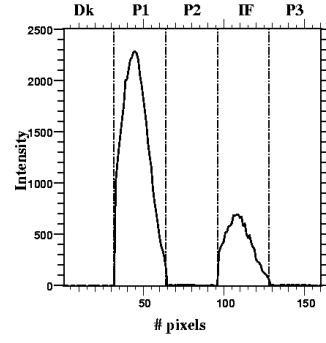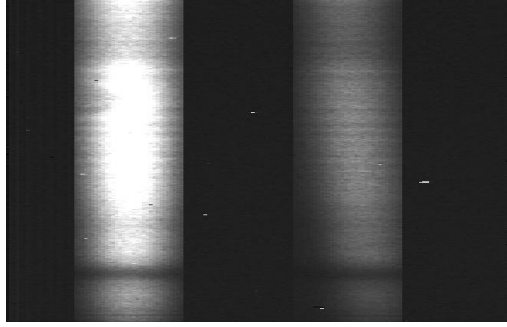
<u>One beam lit</u>

$$p_k^i = F^i b_k^i$$

$$i_k = F^i a_k^i$$

<u>Two beams lit</u>

$$p_k^i = F^i b_k^i$$

$$i_k = F^i a_k^i + F^j a_k^j + \sqrt{a_k^i a_k^j} C_B^{ij} \mathrm{Re} \left[F_c^{ij} \mathrm{e}^{i(2\pi\alpha_k f^{ij} + \phi_s^{ij} + \Phi_B^{ij})} \right]$$
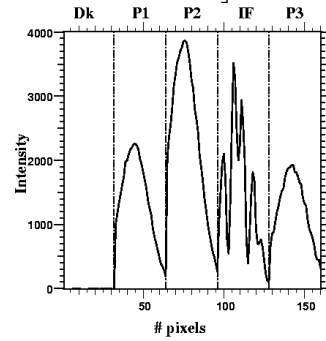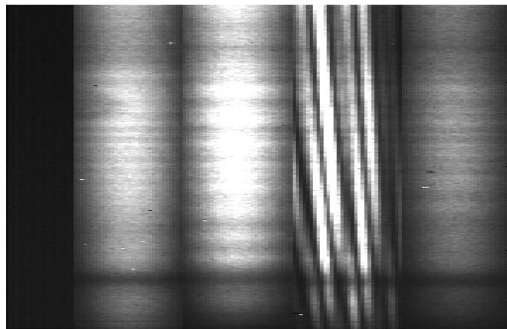
<u>All pairs of beams lit</u>

$$p_k^i = F^i b_k^i$$

$$i_k = \sum_i^{N_{tel}} F^i a_k^i + \sum_{i<j}^{N_{tel}} \sqrt{a_k^i a_k^j} C_B^{ij} \mathrm{Re} \left[F_c^{ij} \mathrm{e}^{i(2\pi\alpha_k f^{ij} + \phi_s^{ij} + \Phi_B^{ij})} \right]$$

6

from now on, and the second sum, which describes the high frequency part (that is the coded fringes), is called the AC component of the interferometric output.

Photometric outputs:

Thanks to the photometric channels, the number of photoevents $p^i(\alpha)$ coming from each telescope can be estimated independently with

$$p_k^i = F^i b_k^i \tag{2}$$

The previous equation rules the photometric channels (resp. columns 2,3,5 of the detector, when illuminated, see table 1).

3.2 Analyzing the AMBER interferometric equation

In order to analyze deeper the content of the AMBER interferometric equation and to use these informations to derive optimized processing of the data, one wants to separate in Eq. (1) the astrophysical and instrumental parts. Furthermore, if we put the DC component on the left side of the equation in order to have on the right side an expression which is linear with respect to the coherent flux, it comes:

$$i_k - \overbrace{\sum_i^{N_{tel}} F^i a_k^i}^{\text{DC component}} = \overbrace{\sum_{i<j}^{N_{tel}} \left[c_k^{ij} R^{ij} + d_k^{ij} I^{ij} \right]}^{\text{AC component}} \tag{3}$$

where

$$c_k^{ij} = C_B^{ij} \frac{\sqrt{a_k^i a_k^j}}{\sqrt{\sum_k a_k^i a_k^j}} \cos(2\pi\alpha_k f^{ij} + \phi_s^{ij} + \Phi_B^{ij}) \tag{4}$$

$$d_k^{ij} = C_B^{ij} \frac{\sqrt{a_k^i a_k^j}}{\sqrt{\sum_k a_k^i a_k^j}} \sin(2\pi\alpha_k f^{ij} + \phi_s^{ij} + \Phi_B^{ij}) \tag{5}$$

are, such as in amplitude modulation techniques of telecom data, called the carrying waves. They only depend on *the characteristics of the instrument,* hence are deterministic[1] and therefore calibratable. On the opposite, the

---

[1] we recall here that thanks to the use of single mode fibers, the intensity profiles a_k^i and b_k^i are fixed and depend only on the configuration of the instrument

quantities:

$$R^{ij} = \sqrt{\sum_k a_k^i a_k^j} \mathrm{Re}\left[F_c^{ij}\right], \quad I^{ij} = \sqrt{\sum_k a_k^i a_k^j} \mathrm{Im}\left[F_c^{ij}\right] \qquad (6)$$

are proportional to the real and imaginary part of the coherent flux. From Eq. (3), it can be seen straightforward that a linear relationship between the *continuum corrected interferograms* and the *complex visibilities* (i.e. from the coherent flux) can be derived, providing that:

(1) the DC component can be estimated: this can be achieved if we know the ratio v_k^i – which only depends on the instrument – between the measured photometric fluxes P^i and the corresponding DC components of the interferogram, that is:

$$a_k^i F^i = P^i v_k^i \qquad (7)$$

where P^i is the estimated photometric flux, integrated over the pixels:

$$P^i = F^i \sum_k b_k^i \qquad (8)$$

(2) the characteristics of the instrument, that is the carrying waves c_k^{ij}, d_k^{ij} are known

As a consequence the AMBER data reduction process consists in *modelling the interferogram* in the detector plane. This requires a previous calibration of the instrument, characterizing the function v_k^i, and the carrying waves c_k^{ij}, d_k^{ij}. The calibration procedure consists in recording a set of so-called calibration files from which the relevant informations (i.e. the v_k^i, c_k^{ij}, and d_k^{ij} functions) can be retrieved, as it is developed in next section.

3.3 The calibration files

The calibration procedure is performed thanks to an internal source located in the *Calibration and Alignment Unit* (CAU) of AMBER (Petrov and the AMBER consortium, 2007). It consists of acquiring a sequence of high signal-to-noise ratio calibration files, whose successive configurations are summarized in Table 2 and explained below. Since the calibration is done in laboratory, the desired level of accuracy for the measurements is insured by choosing the appropriate integration time. As an example, typical integration times in "average accuracy" mode are (for the full calibration process) $\tau = 17s$, 30s, 800s for, respectively, low, medium, and high spectral resolution modes in the K band and 100 times higher for the "high accuracy" calibration mode. The

Table 2
Acquisition sequence of calibration files

Step	Sh 1	Sh 2	Sh 3	Phase γ_0	Step	Sh 1	Sh 2	Sh 3	Phase γ_0
1	O	X	X	NO	5	X	X	O	NO
2	X	O	X	NO	6	O	X	O	NO
3	O	O	X	NO	7	O	X	O	YES
4	O	O	X	YES	8	X	O	O	NO
					9	X	O	O	YES

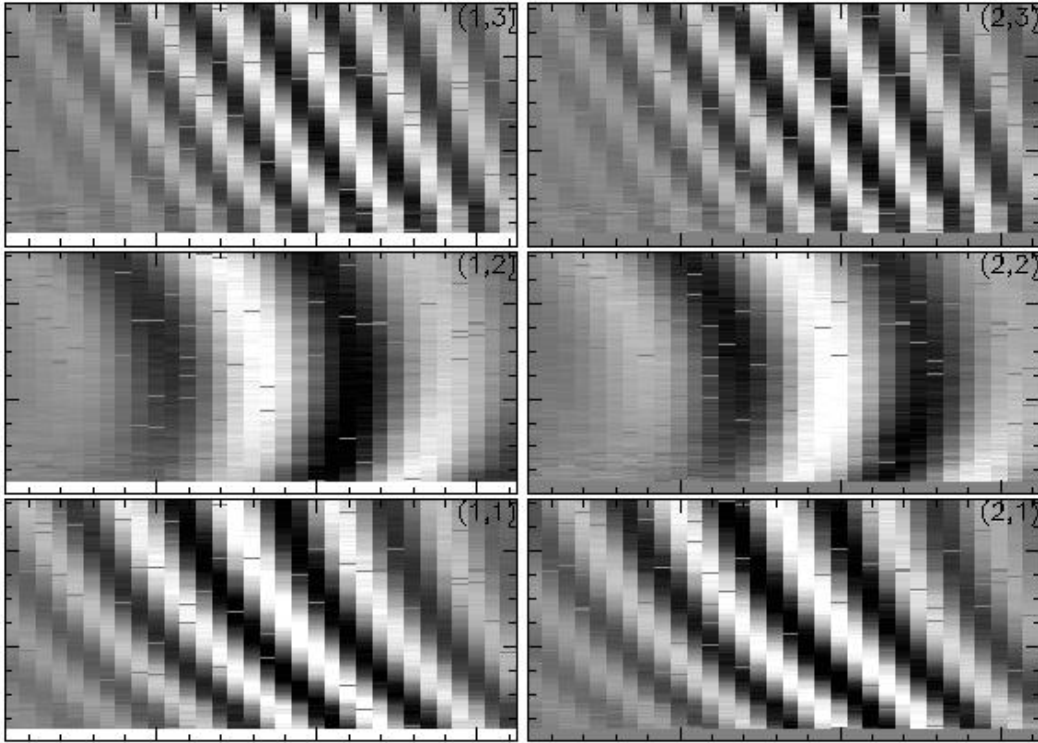Sh = Shutter; O = Open; X = Closed

Fig. 3. Calibrated fringe patterns on the three bases reconstructed from stored calibration files, as shown by the amber-drs software (see sect. B.3.2). From bottom to top: 1-2, 2-3 and 1-3 baselines, left: real part (so-called c_k^{ij}), right: imaginary part (so-called d_k^{ij}).

sequence of calibration files has been chosen to accommodate both two and three-telescope operations. For a two-telescope operation, only the 4 first steps are needed.

v_k^i *estimation: steps* 1 *and* 2 *(and* 5 *when in 3-telescope mode)*
For each telescope beam, an image is recorded with only this shutter opened. The fraction of flux measured between the interferometric channel and the illuminated photometric channel leads to an accurate estimation of the v_k^i functions.
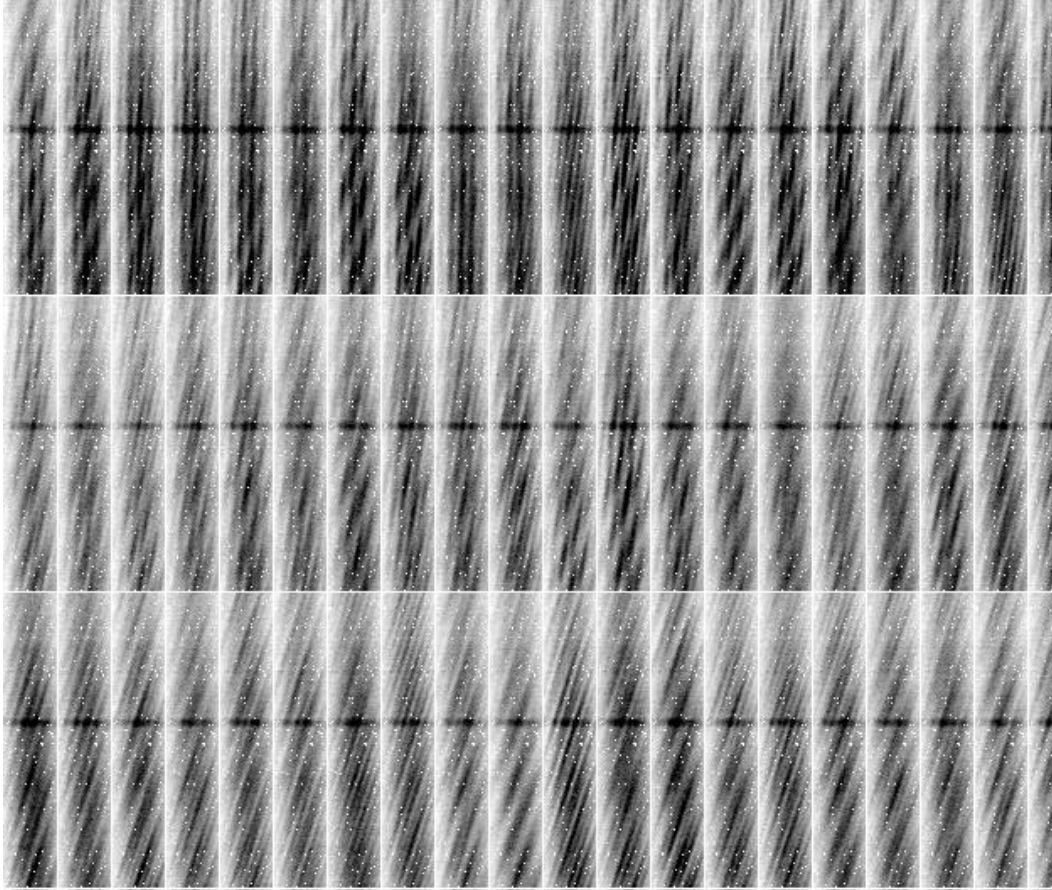
Fig. 4. Sequence of fringes (subset) displayed by the "`Explore data cube with mview`" entry of amber-drs software (see sect. B.3.1). The integration time per frame was 70 ms.

characterization of c_k^{ij} and d_k^{ij} : steps 3/4, 6/7, and 8/9

In order to compute the carrying waves, one needs to have two independent (in terms of algebra) measurements of the interferogram since there are two unknowns (per baseline) to compute. The principle is the following: two shutters are opened simultaneously and for each pair of beams, then the interferogram is recorded on the detector. Such an interferogram corrected for its DC component and calibrated by the photometry yields the knowledge of the c_k^{ij} carrying wave. To obtain its quadratic counterpart, the previous procedure is repeated by introducing a known phase shift close to 90 degree γ_0 using piezoelectric mirrors at the entrance of beams 2 and 3. Computing the d_k^{ij} function from the knowledge of c_k^{ij} and γ_0 is straightforward (see Fig. 3).
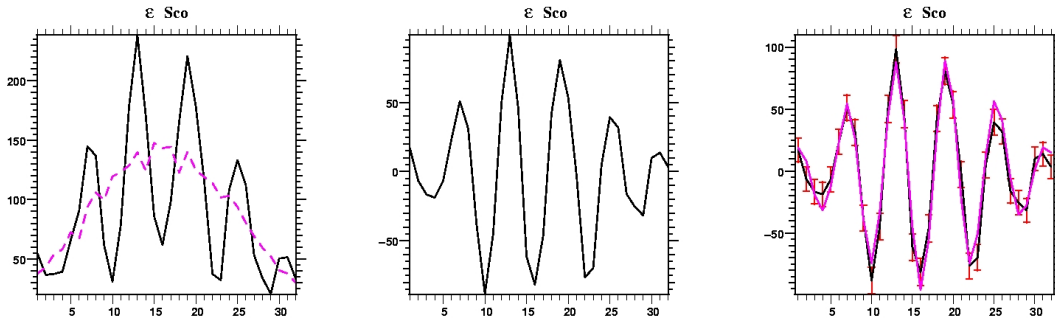
Fig. 5. Steps of the fringe fitting part of the AMBER data reduction. Left: recorded interferogram i_k (DC component over-plotted). Middle: DC component corrected interferogram m_k, now centered around 0. Right: fit of the m_k by the carrying waves.

4 Into science data: getting AMBER observables

Once the calibration files and a sequence of observations (i.e the science data, see an example in Fig. 4) have been recorded, the whole AMBER data reduction process can be performed. The estimation of the AMBER observables requires 4 successive steps:

(1) Cosmetic *(flat-field, sky...)* which converts the infrared CCD in photons counting, a usual procedure that will not be described in further details here
(2) Estimation of the photometric F^i and coherent fluxes F_c^{ij} from the interferograms and the calibration matrix
(3) Derivation of the raw observables
(4) Biases correction

4.1 Estimation of photometric and coherent fluxes

Photometric fluxes – DC subtraction:
As discussed previously, the estimation of the photometric fluxes is straightforward, providing the knowledge of the v_k^i functions (see Eq. (7)). Hence, the DC corrected interferogram, namely m_k, can be computed (Fig. 5, left and middle):

$$m_k = i_k - \sum_{i=1}^{N_{tel}} P^i v_k^i \qquad (9)$$

11

Coherent flux – fringe fitting:
Eq. (9) can then be rewritten:

$$m_k = \sum_{i<j}^{N_{tel}} c_k^{ij} R^{ij} - d_k^{ij} I^{ij} = \underbrace{\left[c_k^{(i,j)}, d_k^{(i,j)} \right]}_{V2PM} \begin{bmatrix} R_{ij} \\ I_{ij} \end{bmatrix} \tag{10}$$

which defines a system of N_{pix} linear equations with $2N_b = N_{tel}(N_{tel} - 1)$ unknowns (i.e. twice the number of baselines). The matrix which contains the $c_k^{(i,j)}$, $d_k^{(i,j)}$ functions is called the V2PM, that stands for *Visibility to Pixel Matrix*. Thus, estimating the real and imaginary parts of the coherent flux requires to solve the inverse problem defined by the matrix-type Eq. (10). Assuming Gaussian statistics for the noise of the measurements m_k, inverting Eq. (10) is done by performing a least square fit of the m_k from the carrying waves, adjusting the R_{ij} and I_{ij} free parameters as shown in Fig. 5, right. Finally, the estimated complex coherent flux C_{ij} comes directly from:

$$C^{ij} = R^{ij} + iI^{ij} = \sqrt{\sum_k a_k^i a_k^j F_c^{ij}} \tag{11}$$

4.2 Estimation of the AMBER observables

The estimated complex coherent flux C_{ij} is directly linked to the complex (modal) visibility of the object through the following equation:

$$C^{ij} \propto F_c^{ij} = 2N\sqrt{t^i t^j} V^{ij} e^{i(\Phi^{ij} + \phi_p^{ij})} \tag{12}$$

Hence, from previous equation one can estimate:

(1) the (squared) modulus of the source's visibility $|V^{ij}|$. This quantity gives informations about the spatial extent of the source, with respect to the chosen baseline
(2) the phase: this latter quantity can not be computed directly because of the atmospheric differential piston ϕ_p^{ij} which adds a random turbulent phase that can not be disentangle from the source one. Fortunately, different ways are available to obtain a partial phase information
  • thanks to the use of 3 telescopes simultaneously, one can compute the so-called *closure phase*, which is independent of the atmosphere. The closure phase gives informations about the geometry of the source, that is the potential asymmetries (e.g. Monnier (2000))
  • thanks to the spectral dispersion offered by the AMBER instrument, the *differential phase* can be estimated as well, leading to the knowledge

12

of the photocenter displacement as a function of the wavelength (Chelli and Petrov, 1995)

The closure phase:
By definition, the closure phase is the phase of the so-called bispectrum B^{123}. The bispectrum results in the ensemble average of the coherent flux triple product and then estimated as

$$\widetilde{B}^{123} = \left\langle C^{12} C^{23} C^{13*} \right\rangle \tag{13}$$

The closure phase then is straightforward:

$$\widetilde{\phi_B}^{\,123} = \text{atan}\left[\frac{\text{Im}(\widetilde{B}^{123})}{\text{Re}(\widetilde{B}^{123})}\right] = \Phi^{12} + \Phi^{23} - \Phi^{13} \tag{14}$$

The closure phase presents the advantage of being independent of the atmosphere (e.g. Roddier (1986)) since the atmospheric piston is a differential quantity, which sum is canceling out when using a closure relation, as it is done in the three telescope case. So far the closure-phase internal error bars (i.e. that does not include systematics errors) are computed statistically by taking the root mean square of all the individual frames, then dividing by the square root of the number of frames.

The differential phase:

The differential phase is the phase of the so-called cross spectrum W_{12}. For each baseline, the latter is estimated from the complex coherent flux taken at two different wavelengths λ_1 and λ_2:

$$\widetilde{W_{12}^{ij}} = \left\langle C_{\lambda_1}^{ij} C_{\lambda_2}^{ij*} \right\rangle \tag{15}$$

And the differential phase is:

$$\widetilde{\Delta\phi_{12}^{ij}} = \text{atan}\left[\frac{\text{Im}\left(\widetilde{W_{12}^{ij}}\right)}{\text{Re}\left(\widetilde{W_{12}^{ij}}\right)}\right] \tag{16}$$

In first order approximation, the differential phase of Eq. (16) is a linear function that takes the generic form $\Delta\phi_{12} = \phi_1 + 2\pi\left(\sigma_2 - \sigma_1\right)\delta$ where $\sigma = 1/\lambda$ is the wavenumber. Its slope $\delta = \delta_p + \delta_o$ depends on the sum of atmospheric piston δ_p, which varies frame by frame, and of the linear component of the object differential phase δ_o. It can be estimated by performing a linear fit of
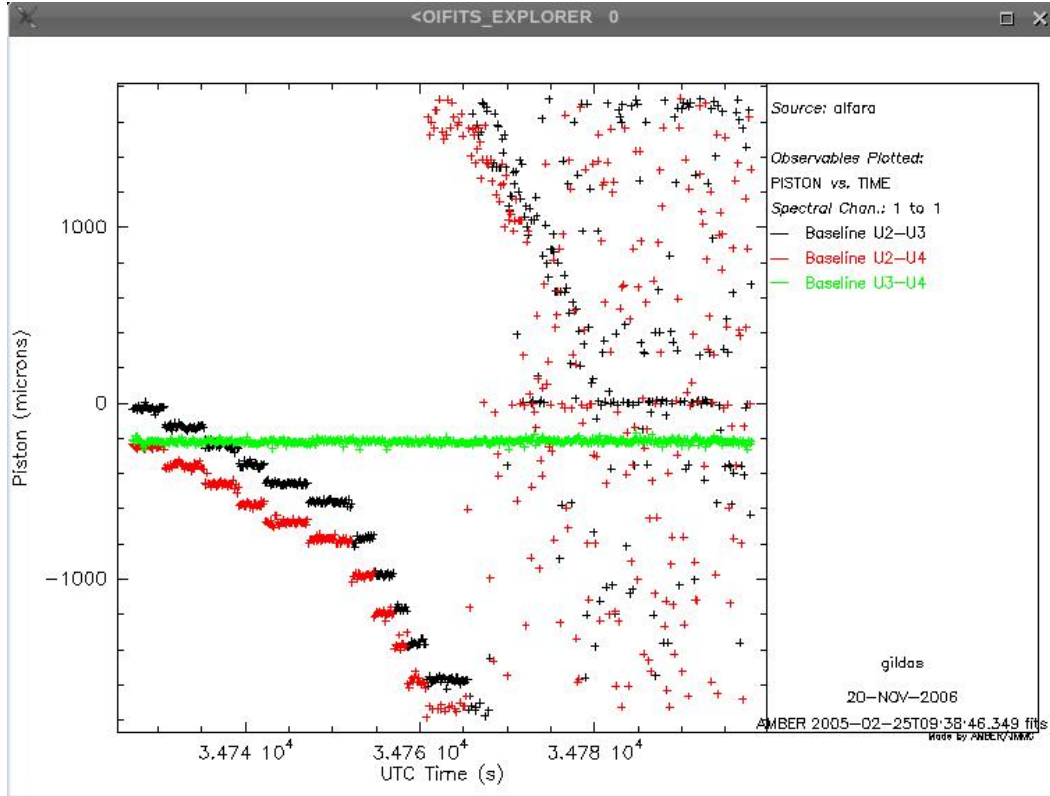
Fig. 6. Behavior of the piston as a function of time for the 3 baselines. This plot is displayed when calling the amber-drs on the appropriate OI-FITS piston file from `gasgano`. See sect. B.4 for details

the differential phase. An illustration is given in Fig. 6. In order to distinguish between the atmospheric piston δ_p and the linear component of the differential phase δ_o, the fitting can be performed by only using spectral channels corresponding to the continuum of the source (i.e. outside spectral features) where the object differential phase is assumed to be zero. An example of differential phase, where the atmospheric piston has been removed using the fitting technique described previously is shown in Fig. 7. Currently, like the closure phase, the internal error bars are computed statistically assuming that the differential phases are statistically independent frame to frame.

The squared visibility:
By definition, the squared visibility is the ratio between the squared coherent flux and the geometrical product of the photometric fluxes. Hence, Eq.'s (6) and (7) tell that the expression of the squared visibility writes:

$$|V^{ij}|^2 = \frac{|F_c^{ij}|^2}{4F^i F^j} = \frac{R^{ij\,2} + I^{ij\,2}}{4P^i P^j \sum_k v_k^i v_k^j} \tag{17}$$

However, one has also to take into account the different biases that are introduced in the estimation of the squared visibilities. The sources of these biases
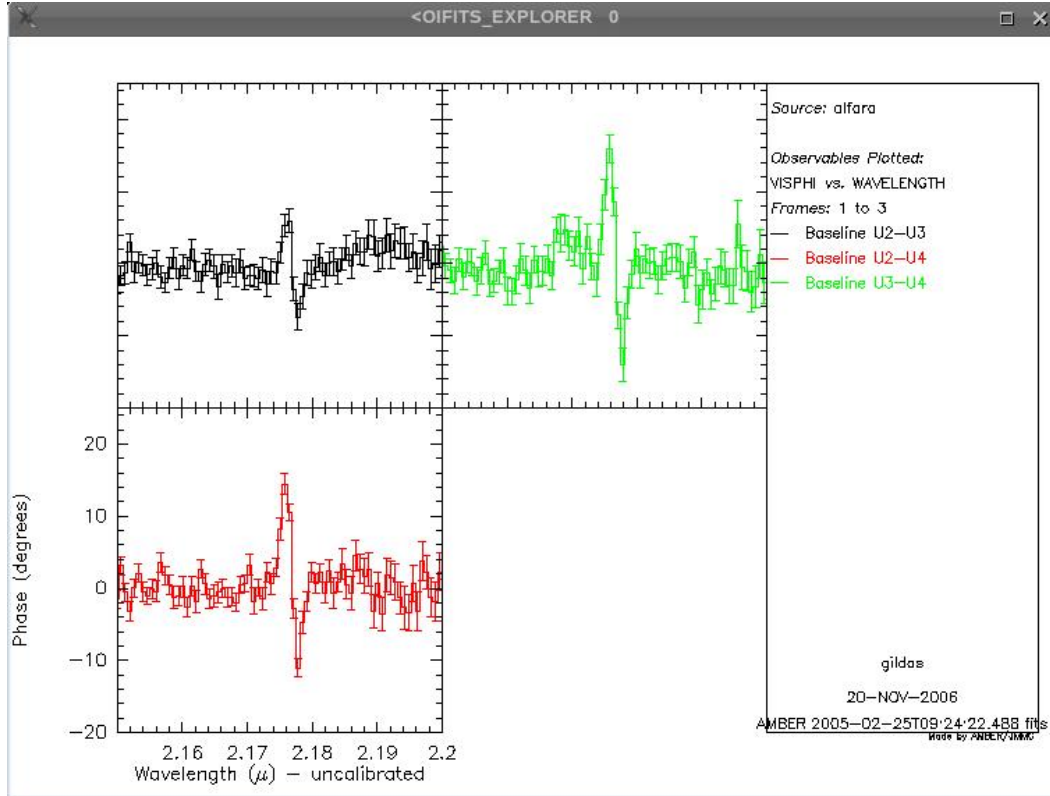
14

Fig. 7. Differential phase as a function of wavelength. Compare with fig. 9 of Meilland and the AMBER consortium (2007). See also sect. B.4.

are:

- the visibility V_c^{ij} of the internal source (CAU), which mediates in the calibration process but not during the observation. This bias is a fixed value and is easily calibratable, e.g. by observing a reference source.
- the quadratic estimation of the coherent flux. Indeed, taking the ensemble average of the squared modulus of the coherent flux introduces an additive bias (Bias$\left\{R^{ij\,2} + I^{ij\,2}\right\}$) due to the zero-mean photon and detector noises (Perrin, 2003). This bias is the quadratic sum of the errors of the measurements $\sigma^2(m_k)$ projected on the real and imaginary axis of the coherent flux. More precisely, if ζ_k^{ij} and ξ_k^{ij} are the coefficients of the generalized inverse of the V2PM matrix, matrix, R^{ik} and I^{ij} verify the respective following equations:

$$R^{ij} = \sum_{k=1}^{N_{pix}} \zeta_k^{ij} m_k, \quad I^{ij} = \sum_{k=1}^{N_{pix}} \xi_k^{ij} m_k \tag{18}$$

Hence, the quadratic bias can then be estimated and subtracted, using:

$$\text{Bias}\{R^{ij\,2} + I^{ij\,2}\} = \sum_k \left[(\zeta_k^{ij})^2 + (\xi_k^{ij})^2\right] \sigma^2(m_k) \tag{19}$$

15

with

$$\sigma^2(m_k) = \overline{i_k} + \sigma^2 + \sum_{i=1}^{N_{tel}} \left[\overline{P_i} + N_{pix}\sigma^2 \right] (v_k^i)^2 \qquad (20)$$

- non zero optical path difference (OPD): since the coherence length $\mathcal{L}_c$ is finite, a non zero OPD induces a loss of spectral coherence that translates into a multiplicative attenuation (ρ_p) of the visibility, which can be computed frame by frame, and corrected using the following formula:

$$\rho_p = \left| \text{sinc}\left(\pi \frac{\delta_p + \delta_o}{\mathcal{L}_c} \right) \right| \qquad (21)$$

δ_p and δ_o being estimated from differential phase measurements, as discussed previously. Note that this effect is usually negligible in medium and high spectral resolution modes, providing typical excursion of the atmospheric piston at Paranal.
- fringe motion during the integration time: it leads to fringe blurring, hence contrast loss (ρ_{jit}), that depends on the features of the turbulent atmosphere, mainly its coherence time. This effect is calibrated by observing a reference star, assuming that the parameters of the turbulence remained the same.

In summary, the estimated visibility verifies the following equation:

$$\underbrace{\frac{\widetilde{|V^{ij}|^2}}{V_c^{ij^2}}}_{CAU\ visibility} = \frac{\left\langle R^{ij^2} + I^{ij^2} \right\rangle \overbrace{-\text{Bias}\left\{ R^{ij^2} + I^{ij^2} \right\}}^{quadratic\ bias}}{4 \left\langle P^i P^j \right\rangle \sum_k v_k^i v_k^j} \underbrace{< \rho_p^2 >}_{piston\ bias} \overbrace{< \rho_{jit}^2 >}^{jitter\ bias} \qquad (22)$$

The associated error of the visibility is computed from the semi-empirical formula, using a second order development of the estimator, following Papoulis (1984):

$$\frac{\sigma^2(\widetilde{|V^{ij}|^2})}{\widetilde{|V^{ij}|^2}^2} = \frac{1}{M} \left[\frac{\langle |C^{ij}|^4 \rangle_M - \langle |C^{ij}|^2 \rangle_M^2}{\langle |C^{ij}|^2 \rangle_M^2} + \frac{\left\langle P^{i2} P^{j2} \right\rangle_M - \langle P^i P^j \rangle_M^2}{\langle P^i P^j \rangle_M^2} \right] \qquad (23)$$

where M is the number of frames used to compute the visibility.

Current limitations:
Due to the present strong vibrations along the VLTI instrumentation (adaptive optics, delay lines, etc.) and the subsequent dysfunction of the FINITO fringe tracker, the fringe contrast is also severely attenuated by a purely instrumental piston, which statistics are unknown and hence, which is potentially

non stationary. As a consequence, it is difficult to insure a reliable absolute calibration of the squared visibility by observing a reference source. The solutions to apply to cope at best with this (hopefully temporary) situation can take two ways:

(1) whether carefully checking the transfer function of the atmosphere+instrument along the night by bracketing the science observations with several calibrator observations, in order to make sure that the transfer function is stable enough to use the usual absolute calibration by a reference source. This is a heavily time consuming solution where a substantial amount of observing time of the science target can be lost

(2) or performing *fringe selection* based on the fringes SNR ratio in order to select only the best fringes (in % of total number of frames), both for the science target and the calibrator, and then taking into account the scatter of frame by frame visibilities in the final error bars. Obviously, such a selection process must be handled with care, and its robustness with regard to the selection level has to be established for any given observation. In other words, for this method to be valid, the expected value for the calibrated visibility must remain the same, with only the error bars changing and eventually reaching a minimum at some specific selection level (see discussion in Tatulli and the AMBER consortium (2007), and the illustration of this effect in the Fig. 6 of the paper). In particular, this method seems well adapted, above all, to cases where the calibrator exhibits a magnitude close to the source's one, where the visibility distribution versus the SNR is expected to behave similarly.

The ESO is currently working hard to identify and suppress these sources of vibrations which are independent on the AMBER instrument. On the issue of these investigations, depends the good operation of the FINITO fringe tracker hence the behavior of the AMBER instrument when dealing with faint sources (e.g. in terms of limiting magnitude).

5 Conclusion

In this paper, we have described and illustrated the data reduction steps that have to undergo VLTI/AMBER interferometric observations. The main specificities of the algorithm to keep in mind are the following: the AMBER signal processing is: (i) a fit of the interferogram in the detector plane, (ii) using an *a priori* calibration of the instrument, where (iii) the complex visibility of the source is estimated from a least-square determination of a linear inverse problem, and where (iv) the derived AMBER observables are the squared visibility, the closure phase, and the spectral differential phase.

A   Notations

Quantity	Definition
k in index	pixel coordinate
α_k	sampling
i, j in exponent	telescope(s)number(s)
p_k^i	photometric channel
i_k	interferometric channel
N	total source photon flux
t^i	total transmission of the ith optical train
a_k^i	intensity profile for the interferometric channel
b_k^i	intensity profile for the photometric channel
f^{ij}	frequency coding
ϕ_s^{ij}	instrumental phase
C_B^{ij}, Φ_B^{ij}	polarization contrast and phase
$F^i = Nt^i$	photometric flux
$F_c^{ij} = 2N\sqrt{t^i t^j} V^{ij} \mathrm{e}^{i(\Phi^{ij} + \phi_p^{ij})}$	coherent flux

B   AMBER data reduction tutorial

Hands on real AMBER data! You have received freshly observed Science Demonstration Time observations of Alpha Arae. In this Practice session we focus on the data quality checks and data reduction.

B.1   Foreword

The complete set of observation files for Alpha Arae (Meilland and the AMBER consortium, 2007), all the programs used here, and download and installation instructions, are present on the Schoolserver.

This tutorial is based on the tools available at the time of the Goutelas School on the computers used by the students. Several utilities described here, and in

particular graphic interfaces (such as `gildas`), may not be in use anymore at the time of reading. The authors expect however that similar tools will be publicly available instead, giving more or less the same feeling of the data.

B.2 A First Look at AMBER Data

Have a look to the contents of the "data" directory, which is "as is" received from ESO. Can you make any sense of it?

The files names are based upon the date/time of delivery in the archive only. What the file really contains is visible only by looking to keywords listed in the file header. The recommended tool to sort and show information on these files is ESO's `gasgano` utility.

B.2.1 Browsing AMBER Data

Call `gasgano`, the ESO tool to browse through the raw data files. Use the `File→Add/Remove File` menu to add the contents of "data". Expand the list of files. In case that the files have been distributed in compressed format, `gasgano` shows only the first (main) FITS header. For normal (uncompressed) files, `gasgano` shows all the headers of the many tables stored in the files (eventually uncompress a file to see this)[2]. How is the data organized?

The data is sorted by time and grouped by object...

---
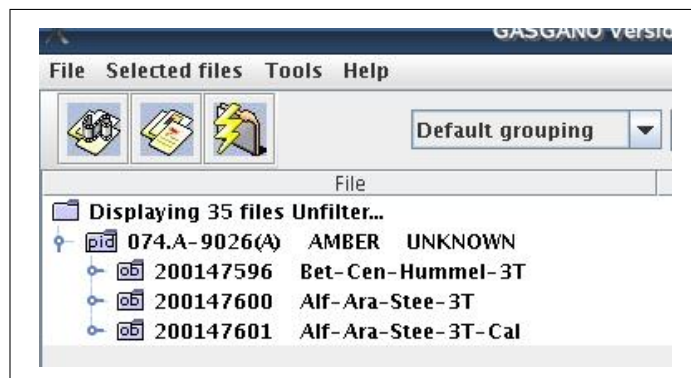
[2] `gasgano` refreshes its directory list only once in a while (depending on a `Preferences...` setup). To view new file, use the `File→Refresh` menu

...Expanding provides the list of files.
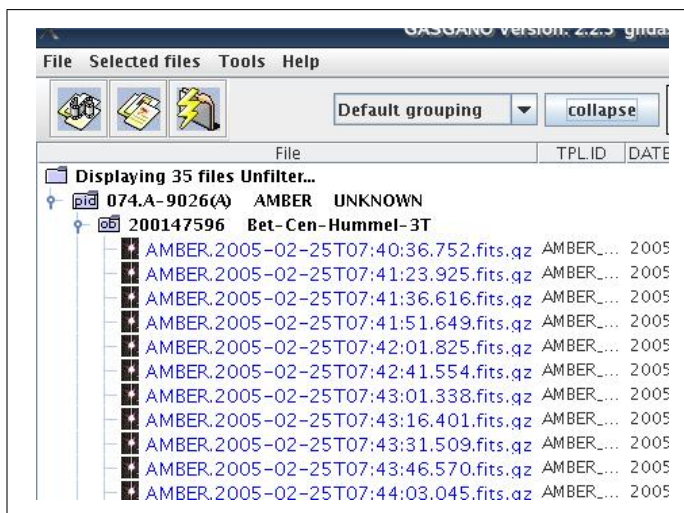
Notice the DPR.CATG and DPR.TYPE values. `gasgano` uses these keywords to classify the files according to instrument-based "classification rules". This classification is used by, e.g., external viewers to adjust their behavior. Why do we have data not pertaining to the "Alf-Ara-Stee-3T" project?

The data contains also the calibration files necessary for "Alf-Ara-Stee-3T", but acquired two hours before during another project. Indeed, files tagged with `DPR.CATG=CALIB` are not proprietary of the observer and are shared among the night's projects. AMBER data sent to an user *should* have all night's calibrators and related calibration files in addition to the project's own `DPR.CATG=SCIENCE` files.

What are the observing modes present in the data? Where are the P2VM raw data files associated with the Alf-Ara observations?
Calibrator: Which calibrator was used for these observations? In total, what are the relevant files for a complete calibrated set of observations (science object + calibrator)?. According to the AMBER data reduction scheme, what calibration steps should be taken and in which order?

- mode: `3Tstd_Medium_K_2.1`, i.e., 3 telescopes, spectral resolution 1000 in K band centered on 2.1 microns.
- P2VM: files are in the `Bet-Cen-Hummel-3T` project.
- Calibrator: `HD165024`

B.2.2   Headers of Raw Data

On an uncompressed file, browse through the various headers with `gasgano`. Better, on any file (zipped or not), call the 'fv' utility to explore the contents
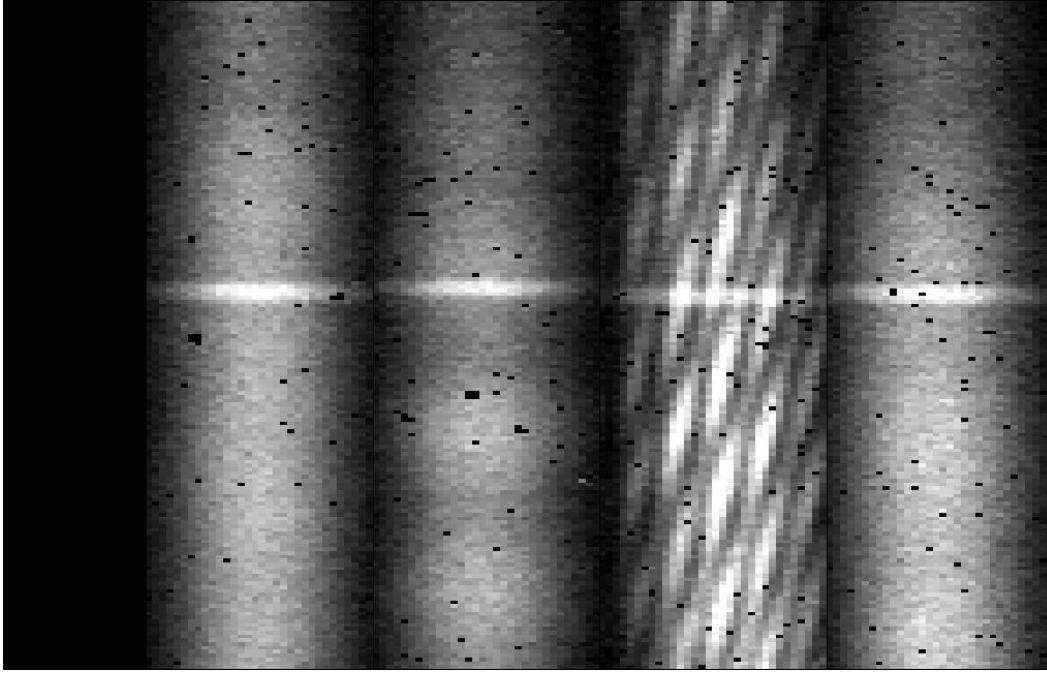
Fig. B.1. The amber-drs displays a raw data file frame with the five area on the detector "glued" together. Notice the emission line in the spectrum and the fringe patterns in the "interferometric window" of the detector.

of the fits file. This can be started with a `gasgano` script. First highlight the filename you want to view, then select the `Script Board` in the `Tools` menu, be sure that the radiobutton `Supply classification is checked`, and double-click on the '`fv.sh`' item in the list.

What are the telescopes used for the file in observing block "200147601"? What is the integration time per frame (DIT)? What indication of the (u,v) values of the baseline are present in the raw data header?

The file with `OBS.ID=200147601` is `AMBER.2005-02-25T10:05:45.944.fits`
- telescopes: `U2 U3 U4`, given by header keys `ISS.CONF.STATION*`
- DIT (Detector Integration Time): 0.07s given by header key `DET.DIT`
- u,v values: `ISS.PBL12.START`, etc... and `ISS.PBLA12.START`, etc... give (start) projected length (resp. angle) of baseline 12 (etc).

B.2.3   View Raw Data Files

Use the "viewfile" Script Board entry to start a gildas-based dedicated viewer (may take some time to start). This external viewer is able to display the contents of raw data files, intermediate calibration files and reduced data files, and changes behavior according to the classification rules. Figure B.1 shows

21

the graphic window of the viewer, displaying the five columns (Masked pixels, photometry 1, photometry 2, interferometry, photometry 3) of the detector. The viewer displays also a floating menu-bar and a panel named "PLOT AMBER DATA FRAMES", that you can use to explore the raw data file.

B.3   Calibrating the Data

B.3.1   Cosmetics

- bad pixel map: The associated Bad Pixel Map is located at `/server/softs/amber/amdmsBadPixelMap.fits.gz`. Use fv to view this file.
- flat-field map: The associated Flat Field Map is located at `/server/softs/amber/amdmsFlatFieldMap.fits`. Use fv to view this file (hint: use histogram equalization). Comment.
- spectral calibration: identify files relates to the (improperly named) spectral calibration step. Eventually run the script `amdlibComputeSpectralCalibration` on the relevant files, and compare values of the *spectral displacement* between interferometric spectrum and photometric spectra ("photometric channels") returned in `/tmp/ComputeSpectralCalibration.log` with the values stored in the following file's headers (keyword 'DET1.P1.OFFSETY').
- perform a "cosmetic calibration only" on a raw data file. This is if you want to check the raw data "images", but is normally not needed by the users. The result file is still a raw data file, but bad pixels have been set to zero, biases and other detector effects removed and the images corrected from flat and gain. Select the file `AMBER.2005-02-25T09:38:46.349.fits.gz`, the accompanying DARK file, and run "amdlibCalibrateRawData".

   This script produce a file in a new directory in the current directory, named "Calibrated". Instruct gasgano to check files in that directory if needed.

   Use "viewFile" to plot the pixels, and the menu item "AMBER VIEWER→Explore data cube with mview" to plot all the fringes in the observation (see example on fig. 4, page 10). What kind of evolution do yo see in the fringe pattern from first frame to the last?

B.3.2   Interferometric Calibration

- view calibration data files.
- build a P2VM: Selecting the relevant set of files, create your first P2VM by using the "amdlibComputeP2vm" script. Use the first available set in the two-telescope data (Medium-K observations), for Low_JHK observations, and for the 3-telescope observations.

- checking a P2VM: after refreshing `gasgano`, view each of the p2vm's content with "viewFile" (opens yet another widget panel, see fig. 3, page 9). In particular, plot the "VK" and "MATRIX" items.

B.4   Compute interferometric Observables

- compute OI-FITS files: Use the amdlibExtractVis script to call the amdlib program of same name to process a science raw data file. Take for example the same raw data file as before, `AMBER.2005-02-25T09:38:46.349.fits.gz`. Note that this script needs only a SCIENCE/OBJECT file and a SCIENCE/DARK file, it finds automatically the corresponding P2VM file.

    This script produce a file in a new directory in the current directory, named "Calibrated". Instruct gasgano to check files in that directory if needed. The filename is the same as the original raw data file, terminated with "_VIS".
- view the results: Use "viewfile" which opens an OI-FITS explorer panel. Almost any entry in an OI-FITS file (which is a 2- or 3-D array) can be viewed against another, with various combinations of frame/spectral channel selections. View especially PISTON vs. TIME [3], VIS2DATA vs. FRINGEQUAL, VIS2DATA vs. WAVELENGTH, differential phases (VISPHI vs. WAVELENGTH, see Fig. 7, page 15), closure phases vs. time.

B.4.1   Frame selection

- **SNR selection**. The script "amdlibComputeAveragedMergedVis" creates OI-FITS files where observables are averaged after frame selection, using a default frame selection criterion based on fringe contrast SNR and a threshold value of 20% best frames. Use and view the corresponding file. For bookkeeping purposes, the result file has the same name as the raw data file, followed by "-XXX-YY_VIS", where XXX is the frame selection criterion (FRG in our default case) and YY the percentage of frames selected according to this criterion (0 to 1).

    By selecting a number of science raw data files, the resulting file is the concatenation of each observation, individually averaged. Experience the results with this script, view the resulting files with "viewFile".
- **Photometry selection**. Waiting for a more flexible `gasgano` interface, this is possible only through the command line mode. Retrieve the (long) command used to create the last OI-FITS file, it is written in the log file `/tmp/ExtractVis.log`. Use it to modify options "-e" and "-r" to suit your purposes. view result with "viewFile".

---

[3] see fig. 6, page 14: the piston on baselines UT2-UT3 and UT2-UT4 decreases dramatically with time because the delay line on UT2 was not moving

B.5 Using the processed data

Under ideal conditions, the frame-selected averaged values should be sufficient for the normal user. However, a few calibrations steps are not provided in the current software:

- correction of visibility loss due to atmospheric piston (large instrumental OPD), and atmospheric piston jitter.
- visibility absolute calibration using a calibrator.

This can be done afterward with any general purpose software equipped with an OI-FITS reader, such as Yorick, IDL, Gildas, etc...

- reading OI-FITS in Yorick
- Averaging in frame, in selection

References

Chelli, A., Petrov, R. G., Feb. 1995. Model fitting and error analysis for differential interferometry. I. General formalism. Astronomy and Astrophysics, Supplement109, 389–399.

Connes, P., Shaklan, S., Roddier, F., 1987. A Fiber-Linked Groundbased Array. In: Goad, J. W. (Ed.), Interferometric Imaging in Astronomy. pp. 165–+.

Coudé du Foresto, V., Faucherre, M., Hubin, N., Gitton, P., Aug. 2000. Using single-mode fibers to monitor fast Strehl ratio fluctuations. Application to a 3.6 m telescope corrected by adaptive optics. Astronomy and Astrophysics, Supplement145, 305–310.

Coudé Du Foresto, V., Ridgway, S., Mariotti, J.-M., Feb. 1997. Deriving object visibilities from interferograms obtained with a fiber stellar interferometer. Astronomy and Astrophysics, Supplement121, 379–392.

Dyer, S. D., Christensen, D. A., Sep. 1999. Pupil-size effects in fiber optic stellar interferometry. Optical Society of America Journal A 16, 2275–2280.

Le Bouquin, J.-B., Tatulli, E., Oct. 2006. Pupil plane optimization for single-mode multi-axial optical interferometry with a large number of telescopes. Mon. Not. of the Royal Astron. Soc.372, 639–645.

Mège, P., Malbet, F., Chelli, A., May 2001. Stellar Interferometry with optical waveguides. In: Societe Francaise d'Astronomie et d'Astrophysique (Ed.), SF2A-2001: Semaine de l'Astrophysique Francaise. pp. 581–+.

Mège, P., Malbet, F., Chelli, A., Feb. 2003. Interferometry with single mode waveguide. In: Traub, W. A. (Ed.), Interferometry for Optical Astronomy II. Edited by Wesley A. Traub. Proceedings of the SPIE, Volume 4838, pp. 329-337 (2003). pp. 329–337.

Meilland, A., the AMBER consortium, 2007. First direct detection of a Keplerian rotating disk around the Be star α Arae using the VLTI/AMBER instrument. Astron. & Astrophys., 4848.

Millour, F., the AMBER consortium, 2007. Direct constraints on the distance of Gamma Velorum based on AMBER/VLTI observations. Astron. & Astrophys., 5408.

Monnier, J. D., 2000. An Introduction to Closure Phases. In: Lawson, P. R. (Ed.), Principles of Long Baseline Stellar Interferometry. pp. 203–+.

Papoulis, A., 1984. Probability, random variables and stochastic processes. New York: McGraw-Hill, 1984, 2nd ed.

Perrin, G., Jan. 2003. Subtracting the photon noise bias from single-mode optical interferometer visibilities. Astron. & Astrophys.398, 385–390.

Petrov, R. G., the AMBER consortium, 2007. AMBER, the near infrared spectro-interferometric three telescopes VLTI instrument. Astron. & Astrophys., 6496.

Roddier, F., Nov. 1986. Triple correlation as a phase closure technique. Optics Communications 60, 145–148.

Shaklan, S., Roddier, F., Jun. 1988. Coupling starlight into single-mode fiber optics. Applied Optics27, 2334–2338.

Tatulli, E., LeBouquin, J.-B., May 2006. Comparison of Fourier and model-based estimators in single-mode multi-axial interferometry. Mon. Not. of the Royal Astron. Soc.368, 1159–1168.

Tatulli, E., Mège, P., Chelli, A., May 2004. Single-mode versus multimode interferometry: A performance study. Astron. & Astrophys.418, 1179–1186.

Tatulli, E., the AMBER consortium, 2007. Interferometric data reduction with VLTI/AMBER. Principle, estimators, and illustration. Astron. & Astrophys., 4799.